Research article

Viscoelastic properties of porcine lenses using optical coherence elastography and inverse finite element analysis

Iulen Cabeza-Gil [a,*], Vahoura Tahsini [b], Sabine Kling [b,c,**]

[a] *Aragón Institute of Engineering Research (i3A), University of Zaragoza, Spain*
[b] *ARTORG Center for Biomedical Engineering Research, University of Bern, Switzerland*
[c] *Institute for Biomedical Engineering, Department of Information Technology and Electrical Engineering, ETH Zurich, Switzerland*

ABSTRACT

The mechanical properties of the crystalline lens are crucial in determining the changes in lens shape that occur during the accommodation process and are also a major factor in the development of the two most prevalent age-related diseases of the lens, presbyopia and cataracts. However, a comprehensive understanding of these properties is currently lacking. Previous methods for characterizing the mechanical properties of the lens have been limited by the amount of data that could be collected during each test and the lack of complex material modeling. These limitations were mainly caused by the lack of imaging techniques that can provide data for the entire crystalline lens and the need for more complex models to describe the non-linear behavior of the lens. To address these issues, we characterized the mechanical properties of 13 porcine lenses during an *ex vivo* micro-controlled-displacement compression experiment using optical coherence elastography (OCE) and inverse finite element analysis (iFEA). OCE allowed us to quantify the internal strain distribution of the lens and differentiate between the different parts of the lens, while iFEA enabled us to implement an advanced material model to characterize the viscoelasticity of the lens nucleus and the relative stiffness gradient in the lens. Our findings revealed a pronounced and rapid viscoelastic behavior in the lens nucleus ($g_1 = 0.39 \pm 0.13$, $\tau_1 = 5.01 \pm 2.31$ s) and identified the lens nucleus as the stiffest region, with a stiffness 4.42 ± 1.20 times greater than the anterior cortex and 3.47 ± 0.82 times greater than the posterior cortex. However, due to the complex nature of lens properties, it may be necessary to employ multiple tests simultaneously for a more comprehensive understanding of the crystalline lens.

1. Introduction

The crystalline lens is one of the two major refractive components of the human eye and the only one that allows to dynamically change its focus. During human accommodation the ciliary muscle contracts, releasing the zonular tension and allowing the lens to increase its curvature (Glasser and Kaufman, 1999). The more curved lens surfaces increase the refractive power of the eye and shift its focus to a closer distance. The change in lens shape is mainly governed by the forces of the lens capsule, and the mechanical properties of the lens nucleus and cortex (Cabeza-Gil et al., 2021a, 2021b). Therefore, an advanced mechanical characterization of the different parts of the lens (nucleus, cortex, and lens capsule) can significantly help to better understand the accommodation mechanism and its two most prevalent age-related diseases, presbyopia and cataracts (Bourne et al., 2021).

Despite the importance of the lens in vision, quantifying the lens mechanical properties *in vivo* remains a challenge due to its high transparency, its high nonlinearity, and the absence of non-invasive testing methods. This could be overcome in the coming years with the emergence of two novel technologies, optical coherence elastography

(OCE) and Brillouin analysis (Ambekar et al., 2020; Besner et al., 2016; Kling, 2021; Kling et al., 2020a,b; Li et al., 2019; Scarcelli et al., 2011). OCE can provide 3D strain maps at high-resolution and with high-acquisition speed (Kennedy et al., 2014; Larin and Sampson, 2017), which can be used to derive the mechanical properties of the tissue. Moreover, due to the nanometer displacement sensitivity, minimal force is required to mechanically stimulate the tissue, ensuring its integrity. On the other hand, Brillouin microscopy can map the longitudinal modulus with microscale resolution. Both technologies are at their early stage and their development is still underway for its clinical application (Larin and Sampson, 2017). The link between the Brillouin shift and viscoelasticity is still unclear (Antonacci et al., 2015). Whereas applying OCE to transparent samples such as the lens is still a challenge because this technique relies on backscattered light (Ambekar et al., 2020). Moreover, quantifying the tissue viscoelasticity with OCE is in its infancy (Larin and Sampson, 2017; Zhang et al., 2022).

Due to the difficulty in measuring the properties of the human lens *in vivo*, the lens has been mostly studied *ex vivo*. Studies have reported that the lens nucleus is softer than the lens cortex in young lenses and becomes stiffer with age with a predominant viscous behavior (Czygan and

---

Hartung, 1996; Heys et al., 2004; Weeber et al., 2005, 2007; Wilde et al., 2012). Those conclusions relied on different mechanical tests (spinning (Reilly et al., 2016; Wilde et al., 2012), localized indentation (Weeber et al., 2007; Reilly and Ravi, 2009), compression (Czygan and Hartung, 1996; Reilly and Cleaver, 2017)) often times in combination with numerical modeling for data interpretation (Weeber and van der Heijde, 2008; Wilde et al., 2012). However, due to the highly nonlinear properties of the lens, characterizing the mechanical properties of the lens nucleus and cortex, and its poro-visco-elasticity remains a challenge. This is due to the large amount of data that needs to be collected and the lack of a complex material model that can accurately describe its complex behavior (Weeber et al., 2005, 2007).

To address these issues, this study aims to characterize the visco-elastic properties of *ex vivo* lenses using OCE and inverse finite element analysis (iFEA). Unlike Brillouin analysis, OCE enables us to quantify strain maps without being biased by the gradient refractive index of the tissue, making it particularly interesting for the study of the crystalline lens. Additionally, the finite element method (FEM) incorporates material parameters such as the Neo-Hookean constant (or Young's modulus), and some time-dependent parameters defined by a Prony Series, that allow us to describe and better understand the complex viscoelastic behavior of the lens. The Neo-Hookean constant represents the stiffness of the lens material whilst Prony Series capture the time-dependent behavior of the lens, accounting for its viscoelastic nature.

2. Methods

OCE is used to quantify the internal strain distribution of the lens whilst FEM serves to corroborate the proposed material model by comparing experimental and numerical results. To achieve this, a sinusoidal micro-displacement was applied to the lens using a piezoelectric actuator, and 3D strain maps were obtained using OCE. These strains were then used to inversely obtain the visco-hyperelastic properties of the lens through iFEA.

Porcine lenses are used in this study, as they are particularly interesting for researchers studying presbyopia. Ungulates, such as pigs, do not accommodate (Caspers, 1979; Duke-Elder, 1958; Vilupuru and Glasser, 2001) and their mechanical properties may resemble those of an aged human lens (Reilly et al., 2016; Schachar et al., 2007), therefore they are considered a good model to study the human mechanism of accommodation.

2.1. Samples

20 freshly-enucleated eyes from 6 to 8 months old pigs were obtained from a local slaughterhouse. Dissection of the lenses was performed within 2–8 h after collection. For this purpose, a scleral incision was made with a surgical scalpel blade and subsequently cornea and sclera were separated with curved micro scissors. The iris, zonules and ciliary were then progressively dissected until the lens was released. Care was taken to not damage the crystalline lenses while extracting it from the eye. Despite, some lenses had to be discarded due to internal damage (n = 3) or technical test problems (n = 4), resulting in 13 lenses tested.

2.2. Experimental tests

The test consisted in axially compressing the lens through a sinusoidal micro-displacement with a period of 5.16 s whilst an optical coherence tomography (OCT) device (Anterion, Heidelberg Enginnering) acquired images at a frequency of 33 Hz, see Fig. 1. The structural OCT image has an axial and lateral resolution of 9.5 μm (in air) and 45 μm, respectively. To apply the sinusoidal micro-displacement, the piezoelectric actuator APF705 (Thorlabs, USA) was used. The test recording period was 7.7 s, over which 256 subsequent B-scans were acquired. The piezoelectric actuator began to displace at 0.8 s from the start of the acquisition.

The piezoelectric actuator was driven with a sinusoidal electrical wave of 16.5 V of amplitude and an offset of 24.5 V. To quantify the actuator micro-displacement and verify it against the manufacturer's unloaded operation curve, an experimental spectral-domain OCT set-up (λ_0 = 878 nm, $\Delta\lambda$ = 62.5 nm, I_{out} = 1.9 mW) described earlier (Kling et al., 2020a,b) was used because of its higher axial resolution (4.48 μm in air). The resulting sine displacement wave had a max. and min. amplitude of 36 (a difference of 8 pixels) and −32 μm (7 pixels), respectively, due to some hysteresis in the piezoelectric actuator.

To characterize a material, the applied force and deformations must be known. Given the difficulty in measuring the force exerted by the lens during micro-sinusoidal displacement (~μg), the lens was axially compressed to 6.00 mm with a step displacement immediately after being extracted from the eye. That is, the compression displacement (Δ) for every lens was calculated as the difference between the initial lens thickness (LT_0) and the compressed thickness (LT_{test}), $LT_{test} = LT_0 - \Delta = 6.00\ mm$, which resulted in an averaged deformation of 15% for the lenses under investigation, also known as pre-strain state of the lenses before conducting the micro-sinusoidal displacement. The force necessary for this compression was measured with a load cell weight sensor
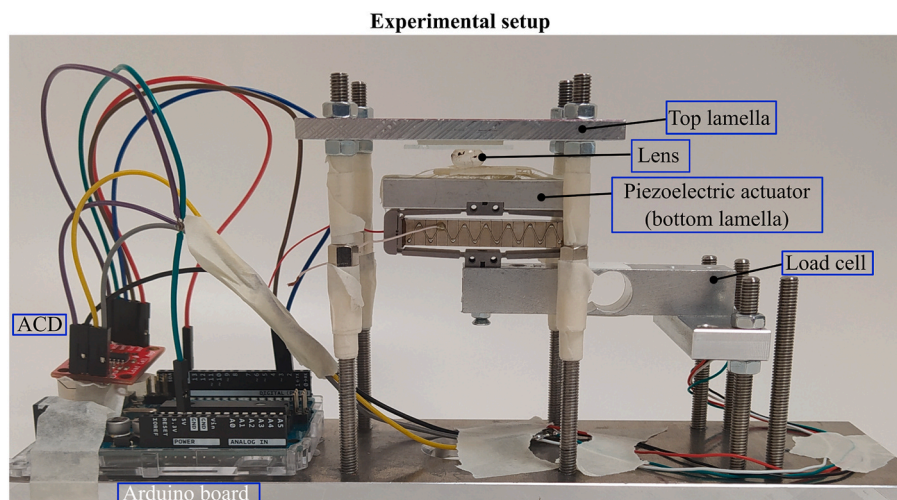
Experimental setup

Fig. 1. Experimental setup. Arduino board registered the values provided by the load cell, which were converted by an analog-to-digital converter (ACD). The piezoelectric actuator was controlled by ARDUINO and an amplifier. The lens was placed between the bottom and top lamella.

(HX711, max. load 1 kg), which was calibrated by a custom script in Arduino using a 10g calibration mass and have a precision of 0.2g.

2.3. Optical coherence elastography

256 cross-sectional OCT scans were processed through custom routines developed in Matlab R2022a (The MathWorks, Inc., Natick, MA, USA) to obtain 2D strain maps of the full central cross-section of the lens. In contrast to earlier literature using OCT for assessing crystalline lens deformation, we interpreted the phase difference between every two consecutively recorded B-scans instead of the intensity distribution in a single structural B-scan. Due to the small deformations induced, the phase reference was maintained from which displacement and finally strain could be derived. Noticeably, the phase-based processing approach allowed a much better signal-to-noise ratio than previous intensity-based approaches, such that despite the high transparency of the tissue, internal lens deformations could be resolved. During post-processing of the complex OCT signal, a similar vector-based phase-sensitive tracking approach was adopted as reported recently (Kling, 2020; Zaitsev et al., 2016) to determine lens strains induced between two subsequent scans. Briefly, the axial displacement Δz (in direction of the optical beam) is calculated as follows:

$$\Delta z = \frac{\lambda \cdot \angle R}{4\pi \cdot n}, \tag{1}$$

being $\lambda = 1300$ nm the mean wavelength of the OCT, $n = 1.49$ the homogeneous refractive index of porcine lens (Vilupuru and Glasser, 2001), and $\angle R$, the angle of the complex cross-correlation calculates as:

$$R = \sum_{j=-w_z}^{w_z} \sum_{k=-w_x}^{w_x} B_S(z+j, x+k) \cdot B_{S+1}^*(z+j, x+k), \tag{2}$$

where B represents an OCT B-scan, B* its complex conjugate, and s = {1, 256} is the number of B-scans. Phase-processing windows with the size $w_z = 10$ and $w_x = 5$. Strain was approximated as the axial gradient and computed by applying a second cross-correlation with the by 1- pixel axially shifted first complex cross-correlation:

$$\varepsilon_z = \frac{\lambda \cdot \angle \sum_{l=-v_z}^{v_z} \sum_{m=-v_x}^{v_x} \left(R_s(z+l, x+m) \cdot R_s^*(z+1+l, x+m) \right)}{4\pi \cdot asu}, \tag{3}$$

being asu = 9.5 μm the axial sampling unit (in air). Note that in contrast to displacement, axial strain measured with OCE is independent of the refractive index. $v_z = 15$ and $v_x = 1$ were the applied strain processing windows.

To obtain the strains of the different regions of the lens (anterior and posterior lens cortex, and lens nucleus), we used 60 lateral pixels in the center of the OCT image and manually selected the boundary regions (anterior-nucleus, and nucleus-posterior) considering the OCT image (Fig. 2a) and the intensity profile (Fig. 2b). Fig. 2b reflects the boundaries used for obtaining the strains in the different lens parts. Processing-windows were applied for noise reduction, which greatly improve image quality, but come at the cost of processing artefacts at the tissue boundaries. In the context of the current study, this needs to be kept in mind when interpreting the deformation in small areas such as the posterior cortex. Due to a higher proportion of boundary pixels and the proximity to two more rigid neighboring regions (nucleus and glass lamella), the posterior cortex might experience a stiffening artefact. To avoid this artefact, care was taken that potentially affected pixels were excluded by defining a distance of 20 pixels from the boundary within which pixels were not considered for subsequent averaging. The pixels encompassing each region were averaged, giving the corresponding strains per region. Moreover, to validate the computed OCE strains, we calculated the average (macroscopic) strain across the entire lens thickness (LT) strains during the controlled-displacement test.

The nucleus delay, which measured the nucleus viscoelasticity, was defined as the time delay between the LT strains and those of the nucleus at the midpoint (t = 2.58 s) of the sinusoidal displacement.

2.4. Finite element model

A 2D axisymmetric finite element (FE) model was developed to simulate the experimental tests. The undeformed geometry consists of the relaxed porcine lens positioned between two lamellae, considered as rigid bodies (Fig. 3a). It was experimentally determined in a representative sample, in which the boundary between nucleus and cortex was particularly well visible in the structural OCT image. The other crystalline geometries were obtained by scaling the reference geometry. Initially the top lamella axially compressed the lens to a thickness of $LT_{test} = LT_0 - \Delta = 6.00$ mm. Then, the experimental sinusoidal microdisplacement was performed by the bottom lamella and the strains were calculated with the compressed lens configuration as reference (Fig. 3b).

Large strains and nonlinearity were considered in this dynamic simulation. The axisymmetric conditions were imposed in the model about the y-axis. A 'hard contact' behavior strictly prohibiting penetration between the lamellae and lens surfaces was applied to maximize the realism of the simulation. No friction was applied. Therefore, the governing equation of the problem was the constitutive equation, together with the equations of force and moment equilibrium:

$$\sigma_{ij} = 2 \frac{\partial y_e}{\partial C_{ij}}, \tag{5}$$

being σ_{ij} the stress tensor, y_e the strain energy density function, and C_{ij}
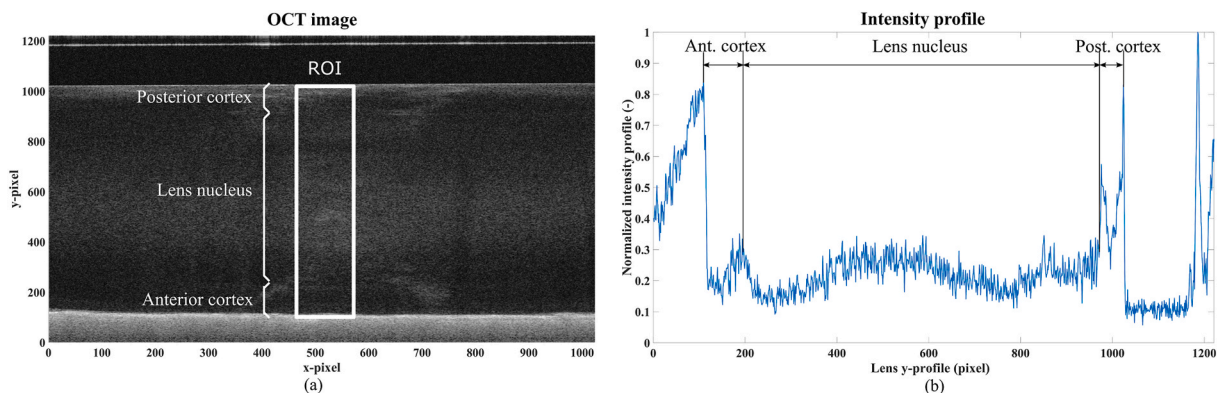

Fig. 2. Structural definitions. (a) representative OCT image and intensity profile (b) highlighting the three parts, posterior cortex, lens nucleus, and anterior cortex. The region of interest (ROI) is indicated in the OCT image.
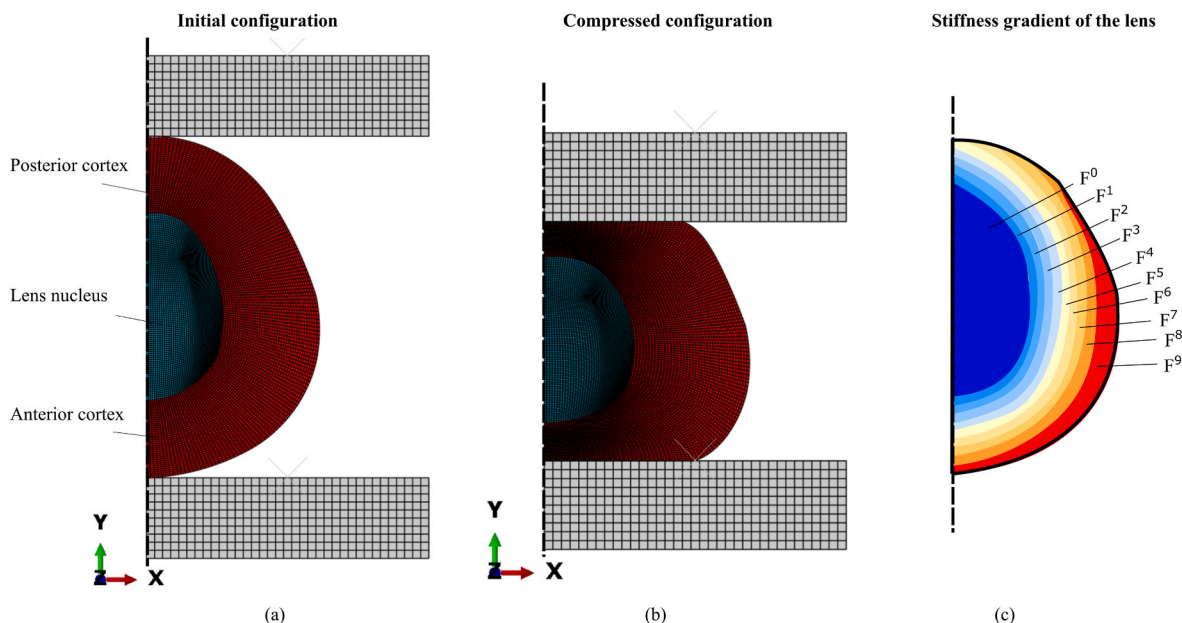
Fig. 3. Finite element model. a) mesh structure of the initial lens geometry. b) mesh structure with the lens in the compressed state. c) stiffness gradient of the lens, implemented by means of 9 cortex layers.

the Green-Cauchy strain tensor. The lens can be considered as a visco-hyperelastic tissue composed of three substances, the nucleus, the cortex, and the lens capsule. The lens nucleus was characterized by an incompressible visco-hyperelastic Neo-Hookean material model due to the large strains (an initial deformation of 15%) applied in the tests (Czygan and Hartung, 1996), described as:

$$y(\mathbf{C}, t) = C_{10}^R(t) \, (I_1 - 3), \tag{6}$$

being $y(\mathbf{C}, t)$ the strain energy density function, $C_{10}^R(t)$ the hyperelastic Neo-Hookean constant and I_1 the first invariant of the right Cauchy-Green deformation tensor, C. The time dependence of $C_{10}^R(t)$ is defined by a one term ($N = 1$) Prony series:

$$C_{10}^R(t) = C_{10}^0 \left(1 - \sum_{i=1}^N g_i \left(1 - e^{-\frac{t}{\tau_i}} \right) \right), \tag{7}$$

$$C_{10}^\infty = C_{10}^0 \left(1 - \sum_{i=1}^N g_i \right), \tag{8}$$

being C_{10}^0 the instantaneous modulus and C_{10}^∞ the long-term modulus. The Prony series parameters are defined by the pre-exponential factor g_1 and the relaxation time τ_1.

For consistency with linear elasticity in small deformations and for comparison across studies, the incompressible Neo-Hookean model can be converted to a linear elastic model with the following relationship:

$$\mu = 2C_{10}, E = 3\mu, \tag{9}$$

being μ the second Lamé parameter, and E, the Young's modulus.

On the other hand, the lens cortex was modeled with a hyperelastic Neo-Hookean material model, without effect of any viscous behavior as we did not observe this behavior in the experimental tests. Moreover, the lens cortex was structured with a non-symmetric stiffness gradient composed of up to 9 concentric layers (de la Hoz et al., 2017; Reilly et al., 2016; Weeber et al., 2007). Because the thickness of the posterior cortex is thinner than the anterior one, it contains only 6 layers. The anterior cortex contains all 9 layers (Fig. 3c).

From nucleus to the external surface, the C_{10}^∞ Neo-Hookean coefficient of every layer was a factor, F, percentage different than the pre-

vious one, $F^n \cdot C_{10-\text{nucleus (N)}}^\infty$, $F^{n+1} \cdot C_{10-N}^\infty \ldots$, being n = 9, the max. number of concentric layers. For instance, if the nucleus has a $C_{10-N}^\infty = 1$ kPa, then with a factor F of 0.9, the cortex layers from the nucleus to the external surface follows this geometric progression: $0.9^n \cdot C_{10-N}^\infty$, $0.9^{n+1} \cdot C_{10-N}^\infty \ldots$, being n = 9, the max. number of layers. To better describe the elasticity of the anterior and posterior cortex, C_{10} was averaged between the layers that compose each part, giving an average $\overline{C}_{10-ANT}$ and $\overline{C}_{10-POST}$.

2.4.1. Influence of the lens capsule in the compression test

Due to the lack of available data of the lens capsule during the compression test, direct characterization was not possible. Instead, our focus shifted to investigating the influence of this unknown factor on the observed internal deformations during the compression test. To analyze this, first we conducted experiments using two numerical models: one with a homogeneous capsule thickness of 60 μm and a Neo-Hookean coefficient of 0.166 MPa (equivalent to a Young's modulus of 1 MPa) (David et al., 2007; Krag et al., 1994), and another without a capsule. By comparing the results between these models, we aimed to understand the impact of the capsule on deformations and applied force. Furthermore, we explored the influence of capsule stiffness and thickness on internal deformations and applied force, varying these parameters to examine their effects within the lens behavior.

2.4.2. Inverse finite element analysis

A response surface was generated to inversely retrieve the mechanical properties for the 13 lenses under investigation. The response surface was generated with a full factorial design according to Table 1,

Table 1
Range of the parameters varied in the full factorial analysis. The LT was varied across the values measured in the study. The others parameter range and levels were chosen based on a prescreening analysis.

Parameter	Thickness (mm)	$g_1(-)$	$\tau_1(s)$	Ratio $\frac{C_{10-N}^\infty}{C_{10-ANT}}$
Levels	3	12	7	20
Values	7.55,7.80,8.10	0.05 to 0.60 in 0.05 steps	0.5, 1, 1.5, 2, 3, 5, 7.5	From a factor, F, of 0.75 to 0.95 in 0.01 steps

involving the thickness of the lens, the Prony series terms of the lens nucleus (g_1, τ_1), and the stiffness ratio $\frac{C_{10-N}^{\infty}}{C_{10-ANT}}$. This resulted in a total of $3 \cdot 12 \cdot 7 \cdot 20 = 5040$ different simulations.

After generating the response surface with the full factorial design, an optimization process was carried out in Matlab to retrieve the mechanical properties of each lens ($\frac{C_{10-N}^{\infty}}{C_{10-ANT}}$, g_1, τ_1) from the experimental values. The optimization was performed by minimizing an error metric defined as the relative average sum of the maximum and minimum strains in the anterior cortex, posterior cortex, and nucleus, along with the viscoelastic delay. All outputs have the same weight. This error metric served as a measure of how well the numerical results match the experimental ones. The response surface optimizer in Matlab was employed to iteratively adjust the input parameters, optimizing them with respect to all these outputs simultaneously. By minimizing the error metric, we aimed to find the optimal set of mechanical properties for every lens that best matched the experimental strain results.

3. Results

3.1. Experimental results

Fig. 4a shows a representative OCE strain map of the compressed lens throughout the test. There is a small dephasing of the strains of the cortex and the nucleus due to the viscoelasticity of the latter. Fig. 4b shows the average strain (LT strain) for all of the compressed porcine lenses under investigation. These data serve as validation of the strains computed by OCE since a controlled-displacement test was performed. Specifically, a maximum and minimum strain of $6.00 \cdot 10^{-3}$ and $5.33 \cdot 10^{-3}$ was applied during the test, whilst the maximum experimental LT strain ranged from $5.56 \cdot 10^{-3}$ to $6.65 \cdot 10^{-3}$ (mean ± std = $6.00 \cdot 10^{-3} \pm 3.65 \cdot 10^{-4}$), and the minimum strain ranged from $4.59 \cdot 10^{-3}$ to $5.93 \cdot 10^{-3}$ (mean ± std = $5.30 \cdot 10^{-3} \pm 4.06 \cdot 10^{-4}$). Fig. 4c–d show a representative compression and tensile OCE cross-sectional strain map of the lens center, respectively. A video of one recording test is also

provided as Supplemental Data.

Fig. 5 shows the averaged strain of the anterior and posterior cortex, and the nucleus for all lenses under investigation. The max. strain in the anterior cortex ranged from $5.62 \cdot 10^{-3}$ to $8.86 \cdot 10^{-3}$ (mean ± std = $7.32 \cdot 10^{-3} \pm 1.13 \cdot 10^{-3}$); the max. nucleus strain ranged from $4.77 \cdot 10^{-3}$ to $7.07 \cdot 10^{-3}$ (mean ± std = $6.11 \cdot 10^{-3} \pm 6.33 \cdot 10^{-4}$); and the max. strain in the posterior cortex ranged from $4.44 \cdot 10^{-3}$ to $6.28 \cdot 10^{-3}$ (mean ± std = $5.37 \cdot 10^{-3} \pm 5.68 \cdot 10^{-4}$). Furthermore, the statistical analysis revealed that the dephasing observed between the cortex (anterior and posterior) and the lens nucleus was statistically significant ($p < 0.001$), highlighting the importance of the viscous behavior of the lens nucleus in the observed phase shift, as illustrated in Fig. 5 (AA section). There was not statistically significant difference between the anterior and posterior cortex ($p = 0.90$).

Fig. 6a and b show the nucleus delay and the maximum force applied to axially compress the lens to 6.00 mm according to the LT. The nucleus delay ranged from $2.50 \cdot 10^{-2}$ to $8.51 \cdot 10^{-2}$ s (mean ± std = $4.66 \cdot 10^{-2} \pm 1.71 \cdot 10^{-2}$ s). The force ranged from 0.51 to 3.76 g-force (gf) (mean ± std = 2.15 ± 0.91 gf) and the LT ranged from 7.55 to 8.10 mm (mean ± std = 7.82 ± 0.16 mm). There was no correlation between the lens nucleus 'delay' and LT ($p = 0.90$) while a statistically significant correlation was found between the force and the LT ($p = 0.009$).

3.2. Numerical results

3.2.1. Influence of the lens capsule in the compression test

The influence of the lens capsule on strains and maximum force was investigated using finite element (FE) models, comparing scenarios with and without the capsule, as depicted in Fig. 7a and b. The findings indicate that the presence of the capsule leads to an increased strain by 22.39% in the nucleus whilst the strains in the anterior and posterior cortex are reduced by 39.37% and 23.54%, respectively, compared to the model without the capsule. Specifically, when considering a lens capsule with a uniform thickness of 60 μm and a Neo-Hookean C_{10}^{∞} constant of 0.166 (equivalent to E = 1.0 MPa) as reported in the
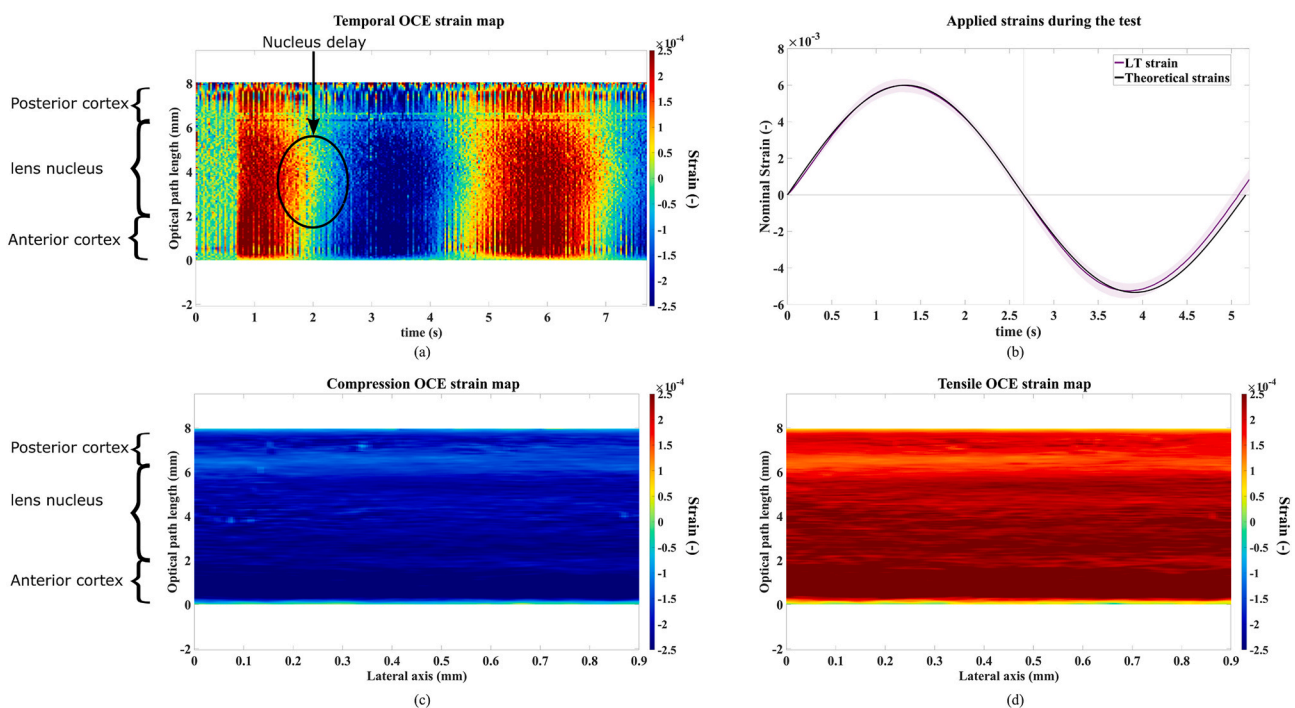

Fig. 4. Strain analysis. a) Temporal OCE strain (−) map of one test averaging the 60 pixels of the lens center. B) Comparison between the averaged and std. strain along the compressed lens thickness for all porcine lenses under investigation for the first 5.16 s of the test after applying piezo displacement and the theoretical strains applied in the controlled-displacement test. c,d) Compression and tensile OCE strain map for lens #5 at the lens center, respectively. The map corresponds to three times the ROI ($60 \times 3 = 180$ pixels).
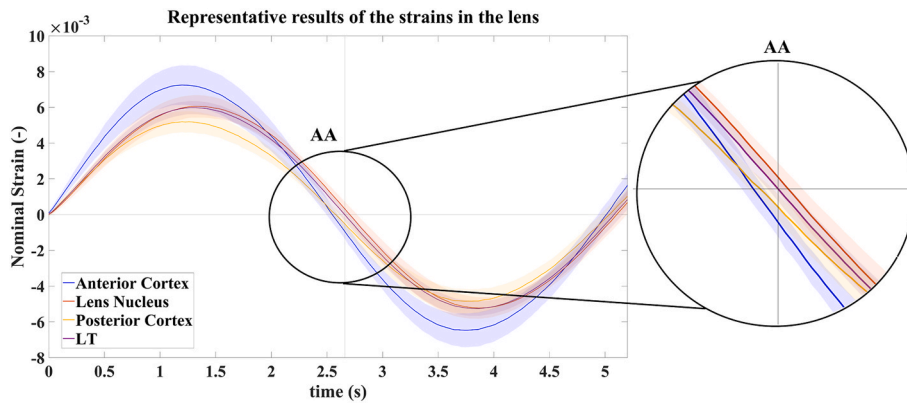
Fig. 5. Experimental data. a) Averaged strain of the anterior and posterior cortex, the lens nucleus, and the compressed lens thickness throughout the sinusoidal micro-displacement for all lenses under investigation (n = 13). Shaded areas represent the standard deviation.
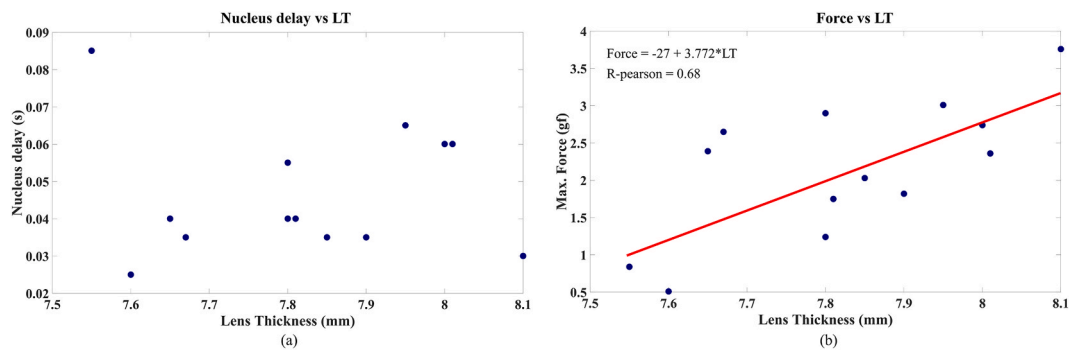

Fig. 6. Correlation of experimental measures according to the porcine lens thickness. a) Nucleus delay (s) against LT. b) maximum force applied to axially compress the lens to 6.00 mm against LT.
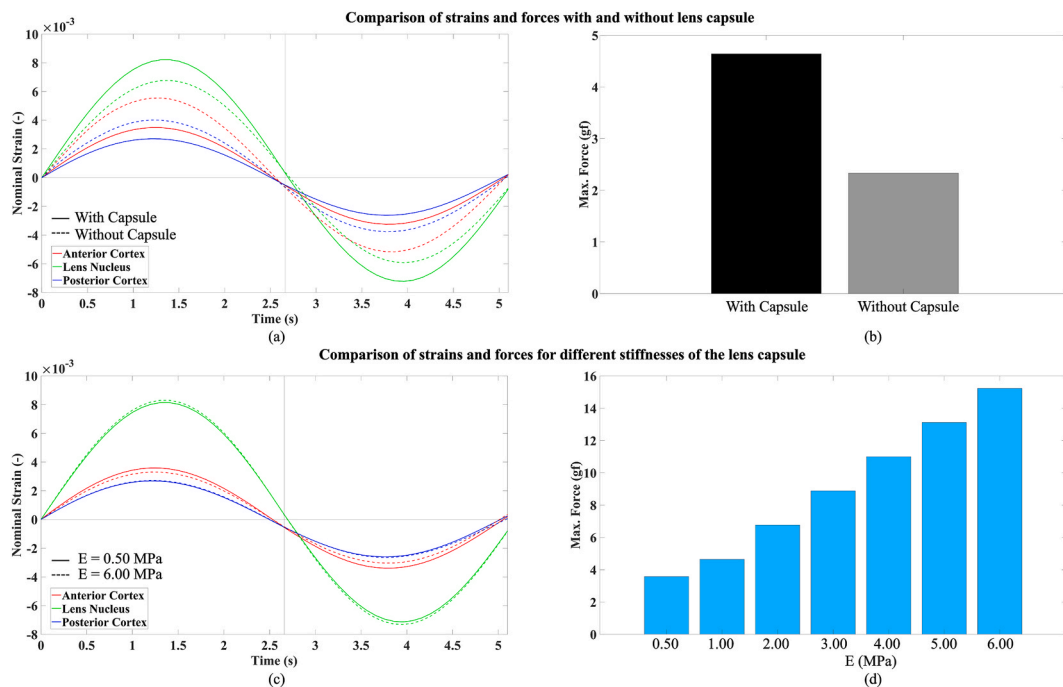

Fig. 7. Comparative analysis of strains (a) and maximum force (b) with and without lens capsule. (c) Influence of capsule stiffness on strains (c) and maximum force (d) within the range of Neo-Hookean constants from 0.50 MPa to 6.00 MPa.

literature (David et al., 2007; Krag et al., 1994), the maximum force is approximately twice as high as that in the model without the capsule (4.64 MPa versus 2.24 MPa).

Due to the limited available data, a comprehensive characterization of the lens capsule in the experimental test was not feasible. Consequently, our investigation focused on examining how the stiffness and thickness of the capsule influence the observed deformations and forces in the test. By employing a homogeneous capsule with a 60 μm thickness (David et al., 2007), we discovered that the internal deformations were nearly identical for C_{10}^{∞} Neo-Hookean model constant stiffness values of 0.083 and 1.00 MPa (Fig. 7c, Young's modulus equivalent of 0.50 MPa and 6.00 MPa, respectively). However, the force values increased as the stiffness of the capsule increased (Fig. 7d). Similar trends were observed for capsules with a Young's Modulus of 1 MPa, encompassing thicknesses ranging from 20 to 90 μm. While the deformations remained consistent, thicker capsules resulted in higher maximum forces.

In the absence of specific information about the lens capsule, we made assumptions and assigned a Neo-Hookean coefficient of 0.166 MPa and a thickness of 60 μm for its characterization (David et al., 2007; Krag et al., 1994). Consequently, extracting the exact mechanical properties of the nucleus and cortex of the crystalline lens from the results of inverse finite element analysis (iFEA) is subject to this assumption. On the other hand, since deformations do not depend on the properties of the capsule, the relative mechanical properties of the tissue (for instance, $\frac{C_{10-N}^{\infty}}{\overline{C}_{10-ANT}}$) can be considered valid.

3.2.2. Mechanical characterization

The visco-hyperelastic properties of the lenses under investigation are gathered in Table 2. The agreement (R^2) between the experimental and numerical strain results ranged from 85 to 99% (mean ± std = 93.72 ± 4.71). The ratio $\frac{C_{10-N}^{\infty}}{\overline{C}_{10-ANT}}$ ranged from 1.34 to 3.24 (mean ± std = 2.61 ± 0.56) whilst the instantaneous ratio $\frac{C_{10-N}^{0}}{\overline{C}_{10-ANT}}$ ranged from 2.73 to 7.28 (mean ± std = 4.42 ± 1.20). A Prony series with one term modeled the viscoelastic behavior of the lens. The term g_1 ranged from 0.17 to 0.60 (mean ± std = 0.39 ± 0.13) whilst the term τ_1 ranged from 0.59 to 7.50 s (mean ± std = 5.01 ± 2.31 s).

With the established properties of the capsule in mind, we can provide an estimation of the absolute mechanical properties of the nucleus and cortex by considering the experimentally applied max force (2.15 gf) during compression and the average parameters fitted ($\frac{C_{10-N}^{\infty}}{\overline{C}_{10-ANT}}$, g_1, τ_1). We submitted several simulations changing the absolute constants of the lens nucleus and cortex (C_{10-N}^{∞}; C_{10-ANT}^{∞}; $C_{10-POST}^{\infty}$), with the same stiffness ratio and Prony series constants, to match the experimental force value. Accordingly, on average the anterior cortex can be approximated with an equivalent Young's modulus (Eq. (9)) of 0.13 kPa, the nucleus of 0.35 kPa (long-term constant), and the posterior cortex of 0.17 kPa.

Fig. 8a and b shows a representative case of the logarithmic strains of the lens and the lens capsule after axial compression to a thickness of 6.00 mm, obtained with the iFEA. The strains were computed with respect to the initial configuration. Fig. 8c shows the corresponding compression and tensile strain computed from the compressed LT deformed configuration. Fig. 8d shows the fitting of a representative numerical case according to the experimental results. Fig. 9 shows three statistically significant correlations (p < 0.01), the ratio $\frac{C_{10-N}^{\infty}}{\overline{C}_{10-N}}$ according to the ratio formed by the max. strains of the lens nucleus and anterior cortex ($\frac{\epsilon_N}{\epsilon_{ANT}}$), $\frac{C_{10-N}^{0}}{\overline{C}_{10-ANT}}$ according to the LT, and τ_1 according to the nucleus delay. There were no further significant correlations among the parameters. The observed correlations in Fig. 9 are subject to the limitation of a small sample size used in our study (n = 13) and may affect the generalizability of the results to a larger population.

3.2.3. Another characterization considering external force data

One strong aspect of our method is its capability to measure all internal strains of the lens, which provided a sufficient amount of data to achieve an optimal and unique solution. However, as experimental noise can affect the reliability of these results, including a force measurement could better confine the solution space. To explore this possibility, we performed additional compression tests on five lenses, with a slightly lower lamellae distance (5.4 mm) to obtain force relaxation data at a lower noise level (Fig. 10 in Supp. Data) and we found a normalized force relaxation of 0.76 ± 0.06 at 15 s after compression.

Since the force relaxation is related to the parameter g_1 and the Neo-Hookean model can be considered as a 'linear material' (Eq. (7)), we set $g_1 = 0.25$ and optimized the results accordingly (Table 3 in Supp. Data). Although the inverse fitting was worse compared to the previous results (90.69% against 93.72%), these optimized results shown in Table 2 could be more reliable considering the aforementioned limitations. The ratio $\frac{C_{10-N}^{\infty}}{\overline{C}_{10-ANT}}$ ranged from 2.33 to 3.24 (mean ± std = 2.96 ± 0.34, against 2.61 ± 0.56 for the optimized results) whilst the instantaneous ratio $\frac{C_{10-N}^{0}}{\overline{C}_{10-ANT}}$ ranged from 3.11 to 4.32 (mean ± std = 3.95 ± 0.45, against 4.42 ± 1.20). τ_1 ranged from 0.5 to 6.01 (mean ± std = 3.45 ± 1.76 s, against 5.01 ± 2.31 s) and there was also a statistically significant correlation between τ_1 and the nucleus delay (p = 0.006).

4. Discussion

The main goal of this study was to demonstrate that the viscoelastic

Table 2

Inverse parameter fitting. Visco-hyperelastic properties of the lenses under investigation. Hyperelastic properties are described by the short- and long-term stiffness ratio nucleus-anterior cortex and the stiffness ratio nucleus-posterior cortex. The visco behavior is modeled by a Prony series. The LT, the theoretical homogeneous (E_{homo}) Young modulus, and the R^2 showing the agreement between the experimental and numerical results is also provided.

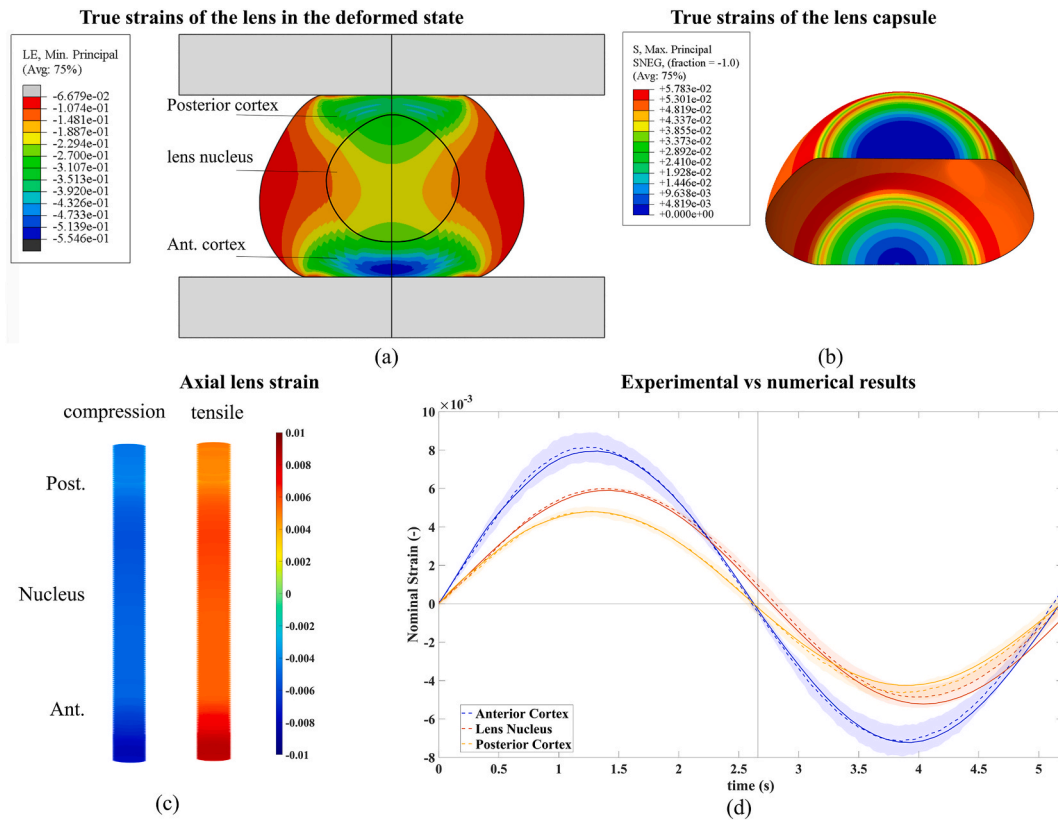|	$\frac{C_{10-N}^{\infty}}{\overline{C}_{10-ANT}}$	$\frac{C_{10-N}^{0}}{\overline{C}_{10-ANT}}$	$\frac{C_{10-N}^{\infty}}{\overline{C}_{10-POST}}$	E_{homo} (kPa)	g_1 (−)	τ_1 (s)	LT (mm)	R^2 (%)
#1	3.24	4.63	2.43	1.16	0.30	0.59	7.55	89
#2	2.83	3.41	2.25	2.14	0.17	2.55	7.81	99
#3	2.35	3.67	1.89	0.68	0.36	7.35	7.60	95
#4	3.02	4.25	2.29	1.52	0.29	6.22	7.80	98
#5	3.11	4.20	2.34	2.15	0.26	6.98	7.90	98
#6	2.21	3.81	1.79	2.45	0.42	7.35	7.85	97
#7	2.91	7.28	2.21	4.12	0.60	7.50	8.10	85
#8	3.24	4.98	2.43	2.67	0.35	2.19	8.01	96
#9	1.87	3.34	1.58	3.46	0.44	4.17	7.67	96
#10	1.34	2.73	1.23	3.15	0.51	7.28	7.65	97
#11	2.76	4.12	2.14	3.57	0.33	3.96	7.80	92
#12	2.72	5.23	2.10	3.11	0.48	3.96	8.00	88
#13	2.35	5.88	1.89	3.49	0.60	5.09	7.95	89

Fig. 8. Inverse modelling results. a) Minimal principal strains of the lens in the compressed configuration. b) Maximal principal strains of the lens capsule in the compressed configuration. The minimal principal strains are proximal to zero, except for the corners of the lens. c) max. absolute compression and tensile strains in the lens center during the micro-sinusoidal displacement. d) Comparative of the experimental (dashed line) and numerical (continuous line) results for the lens #8.
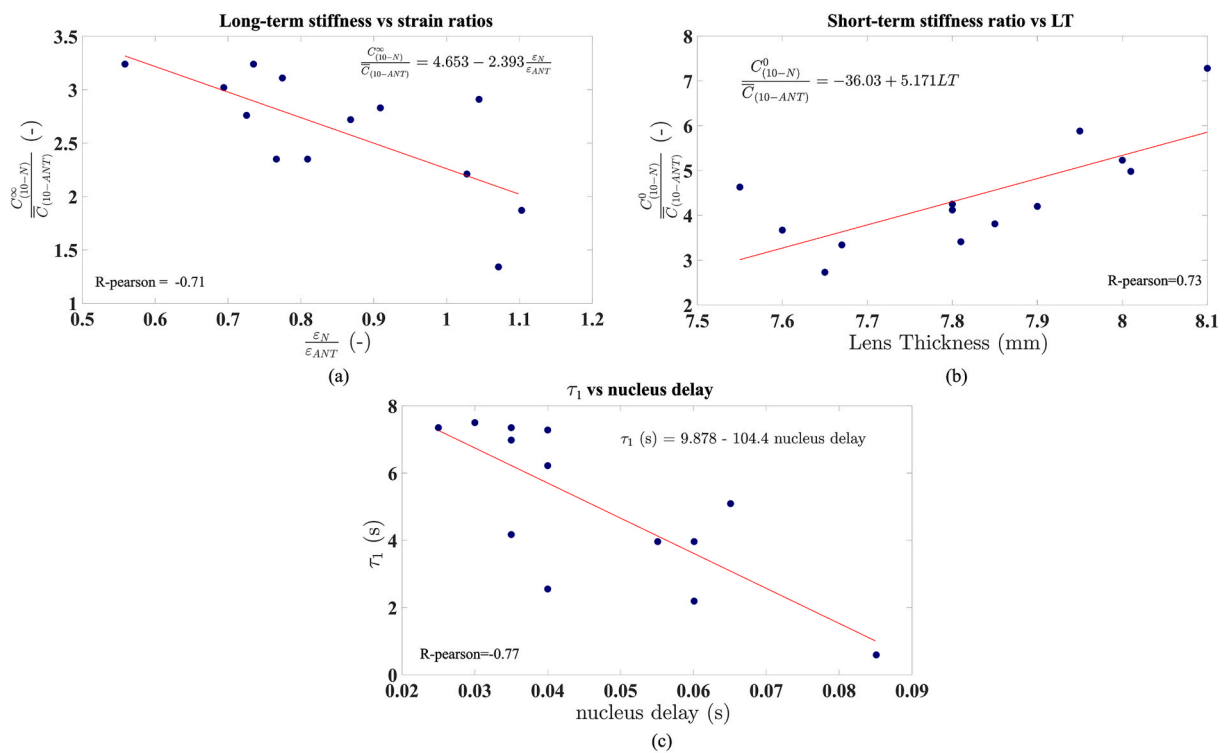

Fig. 9. Correlation of experimental with fitted parameters: a) ratio $\frac{C_{10-N}^{\infty}}{C_{10-ANT}}$ versus LT, and b) Prony series terms versus LT. ratio $\frac{C_{10-N}^{\infty}}{C_{10-ANT}}$ versus $(\frac{\epsilon_N}{\epsilon_{ANT}})$, b) $\frac{C_{10-N}^{0}}{C_{10-ANT}}$ versus LT, and c) vs nucleus delay.

properties of the crystalline lens can be obtained using optical coherence elastography (OCE), and to highlight the importance of using advanced numerical and material models to accurately characterize the non-linear mechanical behavior of the lens. By reproducing experimental data with such models, a more comprehensive understanding of the lens can be gained.

The findings of this study show that the lens nucleus contains a rapid viscoelastic behavior ($g_1 = 0.39 \pm 0.13$, $\tau_1 = 5.01 \pm 2.31$ s). Also, the lens nucleus was identified as the region with the highest stiffness, being approximately 4.42 ± 1.20 times stiffer than the anterior cortex and 3.47 ± 0.82 times stiffer than the posterior cortex in the short-term ($\frac{C_{10-N}^0}{C_{10-ANT}}$; $\frac{C_{10-N}^0}{C_{10-POST}}$). These findings were observed under the applied initial deformation, where the lenses were compressed to a thickness of 6.00 mm. Moreover, we validated the computed OCE strains by comparing them with the theoretical applied strains. The comparison showed a good agreement, with an experimentally observed max. strain along the lens thickness of $6.01 \cdot 10^{-3} \pm 3.62 \cdot 10^{-4}$ against the expected strain of $6.00 \cdot 10^{-3}$ (36 μm/6 mm) that was macroscopically imposed in the controlled-displacement test.

Reilly and Cleaver, 2017 found that the effect of the lens capsule significantly affects the force applied during compression tests. Therefore, we simulated the effect of the capsule on the internal deformations. We also found that it is necessary to include the capsule within the model as the internal deformations differ when the capsule is present compared to when it is absent. The capsule adds another degree of freedom to the problem, making it challenging to fully characterize the entire crystalline lens with the available data. Interestingly, a stiffer or thicker capsule only affects the applied force and not the internal deformations. Therefore, we were able to assume a homogeneous capsule of 60 μm and an equivalent Young's modulus of 1.00 MPa (David et al., 2007) to characterize the tissue with this assumption. The advantage of measuring lens strains using OCE allows us to characterize key parameters, such as the relative stiffness ratio between the nucleus and the anterior ($\frac{C_{10-N}^0}{C_{10-ANT}}$, $\frac{C_{10-N}^\infty}{C_{10-ANT}}$), the relative stiffness ratio between the nucleus and the posterior cortex ($\frac{C_{10-N}^\infty}{C_{10-POST}}$), and the Prony parameters (g_1, τ_1), without being affected by the mentioned capsule assumption. The estimated equivalent Young's modulus for the anterior cortex was 0.13 kPa, for the nucleus was 0.35 kPa (long-term constant), and for the posterior cortex was 0.17 kPa. However, these final absolute values reported are influenced by assumptions imposed on the capsule properties.

Our results are similar to those obtained by (Ambekar et al., 2020) in a study combining OCE and Brillouin analysis, who reported the same tendency for the anterior and posterior lens, and the nucleus with a Young's modulus of 1.98 ± 0.74 kPa, 2.93 ± 1.13 kPa, and 11.90 ± 2.94 kPa, respectively. However, they did not consider the effect of the lens capsule. Other studies have used OCE to measure the lens stiffness (homogeneous Young's modulus) of fresh and cold porcine lenses stimulating the lens by acoustic radiator force (ARF) (Wu et al., 2018; Zhang et al., 2019), reporting values an homogeneous Young's modulus calculation for fresh lenses of ~4 kPa and ~21 kPa for frozen ones. Our results are one magnitude lower. However, the exact properties of the mechanical properties in capsulated lenses are subjected to the assumptions considered for the lens capsule properties.

Other previous studies using traditional methods also reported a similar viscoelastic behavior in human and animal lenses, with a clear rapid viscoelastic term (Czygan and Hartung, 1996; Sharma et al., 2011). As Cyzgan & Hartung, we could confirm that the lens nucleus is responsible for the rapid viscoelastic behavior. The Young's modulus reported through the nucleus and cortex is within the range of values reported by other studies (Reilly et al., 2016; Reilly and Cleaver, 2017; Yoon et al., 2013). Specifically Reilly et al., 2016; Reilly and Cleaver, 2017 reported shear modulus (G, E = 3*G) for decapsulated lenses of ~0.6 kPa, which is in the same order of magnitude of the values reported in this study.

4.1. Limitations

The presence of experimental noise and the absence of dynamic force can hamper the accuracy of the inverse modeling, especially those related to time (viscoelascity). As it might be beneficial to reduce the number of optimization parameters in this case, we conducted two distinct optimizations. As expected, the viscoelastic parameters (g_1, τ_1) changed substantially among the two solutions, however the instantaneous ratio $\frac{C_{10-N}^0}{C_{10-ANT}}$ remained relatively constant (3.95 against 4.42). This confirms the validity of the derived relative mechanical measures in this study.

Another limitation arises from the chosen material model, which likely does not capture every aspect of the crystalline lens' properties. Therefore, the derived material properties are specific to the applied experimental condition, namely a pre-strain of 15%. Future studies quantifying the non-linearity of the lens will permit to further improve the generalizability of our proposed method. In addition, multiple testing methods (spinning, compression, ARF, etc.) might be employed simultaneously to characterize the crystalline lens, as already suggested previously (Reilly and Cleaver, 2017; Weeber et al., 2005, 2007) in order to further enhance the mechanical characterization. Also, with the emergence of new studies shedding light on the biological lens properties, it may be advantageous to explore new approaches that incorporate the movement of water within the lens (poroelasticity) (Chen et al., 2022; Lie et al., 2021). Incorporating poroelastic effects could improve the accuracy of the material model and provide a more comprehensive understanding of the mechanical properties of the crystalline lens (Lavigne et al., 2022).

A minor limitation results from the slightly curved beam propagation through the lens resulting from its gradient refractive index. While the OCT-derived axial strain measure itself is independent of the refractive index, the direction in which strain is assessed depends on the beam propagation through the material. We have minimized this effect of optical distortion by compressing the lens and thus flattening its surfaces and furthermore by considering only the central region of the lens, such that the retrieved strain values can be truly understood as the axial strain component.

5. Conclusions

Optical Coherence Elastography holds promise as a valuable technique for studying the mechanical properties of the crystalline lens. Its ability to quantify internal deformations and its intrinsic feature of the derived strain being independent of the refractive index make it a valuable tool. The main finding of this study is the rapid viscoelasticity of porcine lenses, as well as the higher stiffness of the nucleus compared to the cortex under the tested condition.

Disclosures

The authors declare no conflicts of interest.

Data availability

Data will be made available on request.

Appendix A. Supplementary data

Supplementary data to this article can be found online at https://doi.org/10.1016/j.exer.2023.109558.

References

Ambekar, Y.S., Singh, M., Zhang, J., Nair, A., Aglyamov, S.R., Scarcelli, G., Larin, K.v., 2020. Multimodal quantitative optical elastography of the crystalline lens with optical coherence elastography and Brillouin microscopy. Biomed. Opt Express 11 (4). https://doi.org/10.1364/boe.387361.

Antonacci, G., Pedrigi, R.M., Kondiboyina, A., Mehta, V.v., de Silva, R., Paterson, C., Krams, R., Török, P., 2015. Quantification of plaque stiffness by Brillouin microscopy in experimental thin cap fibroatheroma. J. R. Soc., Interface 12 (112). https://doi.org/10.1098/rsif.2015.0843.

Besner, S., Scarcelli, G., Pineda, R., Yun, S.H., 2016. In vivo brillouin analysis of the aging crystalline lens. Invest. Ophthalmol. Vis. Sci. 57 (13) https://doi.org/10.1167/iovs.16-20143.

Bourne, R.R.A., Steinmetz, J.D., Flaxman, S., Briant, P.S., Taylor, H.R., Resnikoff, S., Casson, R.J., Abdoli, A., Abu-Gharbieh, E., Afshin, A., Ahmadieh, H., Akalu, Y., Alamneh, A.A., Alemayehu, W., Alfaar, A.S., Alipour, V., Anbesu, E.W., Androudi, S., Arabloo, J., et al., 2021. Trends in prevalence of blindness and distance and near vision impairment over 30 years: an analysis for the Global Burden of Disease Study. Lancet Global Health 9 (2). https://doi.org/10.1016/S2214-109X(20)30425-3.

Cabeza-Gil, I., Grasa, J., Calvo, B., 2021a. A numerical investigation of changes in lens shape during accommodation. Sci. Rep. 11 (1) https://doi.org/10.1038/s41598-021-89145-z.

Cabeza-Gil, I., Grasa, J., Calvo, B., 2021b. A validated finite element model to reproduce Helmholtz's theory of accommodation: a powerful tool to investigate presbyopia. Ophthalmic Physiol. Opt. https://doi.org/10.1111/opo.12876.

Caspers, H., 1979. Handbook of sensory physiology. VII/5: the visual system in vertebrates. In: Crescitelli, F. (Ed.), Internationale Revue Der Gesamten Hydrobiologie Und Hydrographie. Springer Verlag, Berlin–Heidelberg–New York, p. 813. https://doi.org/10.1002/iroh.19790640312, 1977. ISBN 3–540-07908-4 (Berlin). 0–387-07908-4 (New York). DM 340,–; US$ 149,60 Vgl. Besprech. Int. Revue ges. Hydrobiol., zuletzt 62 (5).: 698 (1977).

Chen, Y., Petrova, R.S., Qiu, C., Donaldson, P.J., 2022. Intracellular hydrostatic pressure regulation in the bovine lens: a role in the regulation of lens optics? Am. J. Physiol. Regul. Integr. Comp. Physiol. 322 (3) https://doi.org/10.1152/ajpregu.00309.2021.

Czygan, G., Hartung, C., 1996. Mechanical testing of isolated senile human eye lens nuclei. Med. Eng. Phys. 18 (5) https://doi.org/10.1016/1350-4533(95)00076-3.

David, G., Pedrigi, R.M., Heistand, M.R., Humphrey, J.D., 2007. Regional multiaxial mechanical properties of the porcine anterior lens capsule. J. Biomech. Eng. 129 (1) https://doi.org/10.1115/1.2401188.

de la Hoz, A., Scarcelli, G., Yun, S.H., Marcos, S., 2017. Finite element accommodation models using elasticity gradients from Brillouin microscopy. Invest. Ophthalmol. Vis. Sci. 58 (8), 326.

Duke-Elder, S., 1958. *The Eye In Evolution* (Issue V. 1;v. 1958). Mosby. https://books.google.es/books?id=sFr7bwAACAAJ.

Glasser, A., Kaufman, P.L., 1999. The mechanism of accommodation in primates. Ophthalmology 106 (5). https://doi.org/10.1016/S0161-6420(99)00502-3.

Heys, K.R., Cram, S.L., Truscott, R.J.W., 2004. Massive increase in the stiffness of the human lens nucleus with age: the basis for presbyopia? Mol. Vis. 10.

Kennedy, B.F., Kennedy, K.M., Sampson, D.D., 2014. A review of optical coherence elastography: fundamentals, techniques and prospects. IEEE J. Sel. Top. Quant. Electron. 20 (Issue 2) https://doi.org/10.1109/JSTQE.2013.2291445.

Kling, S., 2020. Optical coherence elastography by ambient pressure modulation for high-resolution strain mapping applied to patterned cross-linking. J. R. Soc., Interface 17 (162). https://doi.org/10.1098/rsif.2019.0786.

Kling, S., 2021. In-vivo measurement of ocular deformation in response to ambient pressure modulation. Front. Bioeng. Biotechnol. 9 https://doi.org/10.3389/fbioe.2021.759588.

Kling, S., Khodadadi, H., Goksel, O., 2020a. Optical coherence elastography-based corneal strain imaging during low-amplitude intraocular pressure modulation. Front. Bioeng. Biotechnol. 7 https://doi.org/10.3389/fbioe.2019.00453.

Kling, S., Torres-Netto, E.A., Spiru, B., Sekundo, W., Hafezi, F., 2020b. Quasi-static optical coherence elastography to characterize human corneal biomechanical properties. Invest. Ophthalmol. Vis. Sci. 61 (6) https://doi.org/10.1167/IOVS.61.6.29.

Krag, S., Thim, K., Corydon, L., Kyster, B., 1994. Biomechanical aspects of the anterior capsulotomy. J. Cataract Refract. Surg. 20 (4) https://doi.org/10.1016/S0886-3350(13)80176-9.

Larin, K.v., Sampson, D.D., 2017. Optical coherence elastography – OCT at work in tissue biomechanics [Invited]. Biomed. Opt Express 8 (2). https://doi.org/10.1364/boe.8.001172.

Lavigne, T., Sciume, G., Laporte, S., Pillet, H., Urcun, S., Wheatley, B., Rohan, P.Y., 2022. Société de Biomécanique Young Investigator Award 2021: numerical investigation of the time-dependent stress–strain mechanical behaviour of skeletal muscle tissue in the context of pressure ulcer prevention. Clin. BioMech. 93 https://doi.org/10.1016/j.clinbiomech.2022.105592.

Li, Y., Zhu, J., Chen, J.J., Yu, J., Jin, Z., Miao, Y., Browne, A.W., Zhou, Q., Chen, Z., 2019. Simultaneously imaging and quantifying in vivo mechanical properties of crystalline lens and cornea using optical coherence elastography with acoustic radiation force excitation. APL Photonics 4 (10). https://doi.org/10.1063/1.5118258.

Lie, A.L., Pan, X., White, T.W., Vaghefi, E., Donaldson, P.J., 2021. Age-dependent changes in total and free water content of in vivo human lenses measured by magnetic resonance imaging. Invest. Ophthalmol. Vis. Sci. 62 (9) https://doi.org/10.1167/iovs.62.9.33.

Reilly, M.A., Cleaver, A., 2017. Inverse elastographic method for analyzing the ocular lens compression test. J. Innovat. Optical Health Sci. 10 (6) https://doi.org/10.1142/S1793545817420093.

Reilly, M.A., Martius, P., Kumar, S., Burd, H.J., Stachs, O., 2016. The mechanical response of the porcine lens to a spinning test. Zeitschrift Fur Medizinische Physik 26 (2). https://doi.org/10.1016/j.zemedi.2015.12.009.

Reilly, M., Ravi, N., 2009. Microindentation of the young porcine ocular lens. ASME. J Biomech Eng. 131 (4), 044502. https://doi.org/10.1115/1.3072891.

Scarcelli, G., Kim, P., Yun, S.H., 2011. In vivo measurement of age-related stiffening in the crystalline lens by Brillouin optical microscopy. Biophys. J. 101 (6) https://doi.org/10.1016/j.bpj.2011.08.008.

Schachar, R.A., Chan, R.W., Fu, M., 2007. Viscoelastic shear properties of the fresh porcine lens. Br. J. Ophthalmol. 91 (3) https://doi.org/10.1136/bjo.2006.105965.

Sharma, P.K., Busscher, H.J., Terwee, T., Koopmans, S.A., van Kooten, T.G., 2011. A comparative study on the viscoelastic properties of human and animal lenses. Exp. Eye Res. 93 (5) https://doi.org/10.1016/j.exer.2011.08.009.

Vilupuru, A.S., Glasser, A., 2001. Optical and biometric relationships of the isolated pig crystalline lens. Ophthalmic Physiol. Opt. 21 (4) https://doi.org/10.1016/S0275-5408(00)00057-0.

Weeber, H.A., Eckert, G., Pechhold, W., van der Heijde, R.G.L., 2007. Stiffness gradient in the crystalline lens. Graefe's Arch. Clin. Exp. Ophthalmol. 245 (9) https://doi.org/10.1007/s00417-007-0537-1.

Weeber, H.A., Eckert, G., Soergel, F., Meyer, C.H., Pechhold, W., Van Der Heijde, R.G.L., 2005. Dynamic mechanical properties of human lenses. Exp. Eye Res. 80 (3) https://doi.org/10.1016/j.exer.2004.10.010.

Weeber, H.A., van der Heijde, R.G.L., 2008. Internal deformation of the human crystalline lens during accommodation. Acta Ophthalmol. 86 (6) https://doi.org/10.1111/j.1600-0420.2007.01116.x.

Wilde, G.S., Burd, H.J., Judge, S.J., 2012. Shear modulus data for the human lens determined from a spinning lens test. Exp. Eye Res. 97 (1) https://doi.org/10.1016/j.exer.2012.01.011.

Wu, C., Aglyamov, S.R., Han, Z., Singh, M., Liu, C.-H., Larin, K.v., 2018. Assessing the biomechanical properties of the porcine crystalline lens as a function of intraocular pressure with optical coherence elastography. Biomed. Opt Express 9 (12). https://doi.org/10.1364/boe.9.006455.

Yoon, S., Aglyamov, S., Karpiouk, A., Emelianov, S., 2013. The mechanical properties of ex vivo bovine and porcine crystalline lenses: age-related changes and location-dependent variations. Ultrasound Med. Biol. 39 (6) https://doi.org/10.1016/j.ultrasmedbio.2012.12.010.

Zaitsev, V.Y., Matveyev, A.L., Matveev, L.A., Gelikonov, G.v., Sovetsky, A.A., Vitkin, A., 2016. Optimized phase gradient measurements and phase-amplitude interplay in optical coherence elastography. J. Biomed. Opt. 21 (11) https://doi.org/10.1117/1.jbo.21.11.116005.

Zhang, H., Singh, M., Zvietcovich, F., Larin, K., Aglyamov, S., 2022. Age-related changes in the viscoelasticity of rabbit lens characterised by surface wave dispersion analysis. Quant. Electron. 52 (1) https://doi.org/10.1070/qel17964.

Zhang, H., Wu, C., Singh, M., Nair, A., Aglyamov, S.R., Larin, K.v., 2019. Optical coherence elastography of cold cataract in porcine lens. J. Biomed. Opt. 24 (3) https://doi.org/10.1117/1.jbo.24.3.036004.